Nanoconfined Water in Magnesium-Rich 2:1 Phyllosilicates

Nathan W. Ockwig,[†] Jeffery A. Greathouse,*,[†] Justin S. Durkin,[†] Randall T. Cygan,[†]
Luke L. Daemen,[‡] and Tina M. Nenoff[§]

Geochemistry Department and Surface and Interface Sciences Department, Sandia National Laboratories, P.O. Box 5800, Albuquerque, New Mexico 87185 and Manuel Lujan, Jr. Neutron Scattering Center LANSCE-LC, Los Alamos National Laboratory, P.O. Box 1663, Los Alamos, New Mexico 87545

Received February 2, 2009; E-mail: jagreat@sandia.gov

Abstract: Inelastic neutron scattering, density functional theory, ab initio molecular dynamics, and classical molecular dynamics were used to examine the behavior of nanoconfined water in palygorskite and sepiolite. These complementary methods provide a strong basis to illustrate and correlate the significant differences observed in the spectroscopic signatures of water in two unique clay minerals. Distortions of silicate tetrahedra in the smaller-pore palygorskite exhibit a limited number of hydrogen bonds having relatively short bond lengths. However, without the distorted silicate tetrahedra, an increased number of hydrogen bonds are observed in the larger-pore sepiolite with corresponding longer bond distances. Because there is more hydrogen bonding at the pore interface in sepiolite than in palygorskite, we expect librational modes to have higher overall frequencies (i.e., more restricted rotational motions); experimental neutron scattering data clearly illustrates this shift in spectroscopic signatures. It follows that distortions of the silicate tetrahedra in these minerals effectively disrupt hydrogen-bonding patterns at the silicate−water interface, and this has a greater impact on the dynamical behavior of nanoconfined water than the actual size of the pore or the presence of coordinatively unsaturated magnesium edge sites.

Introduction

Water is an essential component in many environmental systems and industrial processes involving porous materials. Characterizing the behavior of water confined in such materials is crucial to advance our understanding of macroscopic phenomena (i.e., species mobility, ultrafiltration, ion exchange, adsorption, etc.). These efforts ultimately provide a foundation for modifying or even potentially directing such properties to serve a specifically engineered purpose.

Although the properties and behaviors of bulk water are generally understood, under nanoconfined conditions these topics are perplexing challenges which tax even the most sophisticated levels of theory.[1−4] Structural and dynamical properties of bulk water have been studied over an impressive temperature and pressure range, while comparatively few studies have focused on the unique properties and characteristics of water confined in porous materials.[5−17] Nevertheless, it is well documented that

the differences between bulk and nanoconfined water are very significant.[18−29] Herein, we expand these studies to include magnesium-rich 2:1 phyllosilicate clay minerals, specifically palygorskite and sepiolite.[30−37] Although these phases have very similar architectures, our results show that subtle differences in the structure and organization of nanoconfined water result in significant differences in dynamics and experimental inelastic neutron scattering (INS) spectra.

- (7) Ludwig, R. *Angew. Chem., Int. Ed.* **2001**, *40*, 1808.
- (8) Coe, J. V. *Int. Rev. Phys. Chem.* **2001**, *20*, 33.
- (9) Hare, D. E.; Sorenson, C. M. *J. Chem. Phys.* **1990**, *93*, 25.
- (10) Coe, J. V.; Earhart, A. D.; Cohen, M. H.; Hoffman, G. J.; Sarkas, H. W.; Bowen, K. H. *J. Phys. Chem.* **1997**, *107*, 6023.
- (11) Silvestrelli, P. L.; Parrinello, M. *J. Chem. Phys.* **1999**, *111*, 3572.
- (12) Kukulka, D. J.; Gebhart, B.; Mollendorf, J. C. *Adv. Heat Transfer* **1987**, *18*, 325.
- (13) Burnham, C. W.; Holloway, J. R.; Davis, N. F. *Geol. Soc. Am. Spec. Pap.* **1969**, *132*, 96.
- (14) Speedy, R. J. *J. Phys. Chem.* **1982**, *86*, 982.
- (15) Hill, P. G. *J. Phys. Chem. Ref. Data* **1990**, *19*, 1233.
- (16) Wallqvist, A.; Åstrand, P. O. *J. Chem. Phys.* **1995**, *102*, 6559.
- (17) Zielkiewicz, J. *J. Chem. Phys.* **2005**, *123*, 104501.
- (18) Rovere, M. *J. Phys.: Condens. Matter, Spec. Sect. Water Confined Geometries* **2004**, *16*, S5297.
- (19) Crupi, V.; Majolino, D.; Venuti, V. *J. Phys.: Condens. Matter, Spec. Sect. Water Confined Geometries* **2004**, *16*, S5297.
- (20) Swenson, J. *J. Phys.: Condens. Matter, Spec. Sect. Water Confined Geometries* **2004**, *16*, S5317.
- (21) Puibasset, J.; Pellenq, R. J. M. *J. Phys.: Condens. Matter, Spec. Sect. Water Confined Geometries* **2004**, *16*, S5329.
- (22) Brovchenko, I.; Geiger, A.; Oleinikova, A. J. *J. Phys.: Condens. Matter, Spec. Sect. Water Confined Geometries* **2004**, *16*, S5345.
- (23) Zangi, R. *J. Phys.: Condens. Matter, Spec. Sect. Water Confined Geometries* **2004**, *16*, S5371.
- (24) Jedlovsky, P. *J. Phys.: Condens. Matter, Spec. Sect. Water Confined Geometries* **2004**, *16*, S5389.

- [†] Geochemistry Department, Sandia National Laboratories.
- [‡] Los Alamos National Laboratory.
- [§] Surface and Interface Sciences Department, Sandia National Laboratories.

- (1) Angell, C. A. In *Water: A Comprehensive Treatise*; Franks, F., Ed.; Plenum Press: New York, 1981.
- (2) Klafter, J.; Blumen, A.; Drake, J. M. In *Relaxation and Diffusion in Restricted Geometry*; Klafter, J., Drake, J. M., Eds.; Wiley: New York, 1989.
- (3) Rupley, J. A.; Careri, G. *Adv. Protein Chem.* **1991**, *41*, 37.
- (4) Arndt, M.; Stannarius, R.; Gorbatschow, W.; Kremer, F. *Phys. Rev. E* **1996**, *54*, 5377.
- (5) Kell, G. S. *J. Chem. Eng. Data* **1967**, *12*, 66.
- (6) Sansom, M.; Kerr, I.; Breed, J.; Sankararamakrishnan, R. *Biophys. J.* **1996**, *70*, 693.
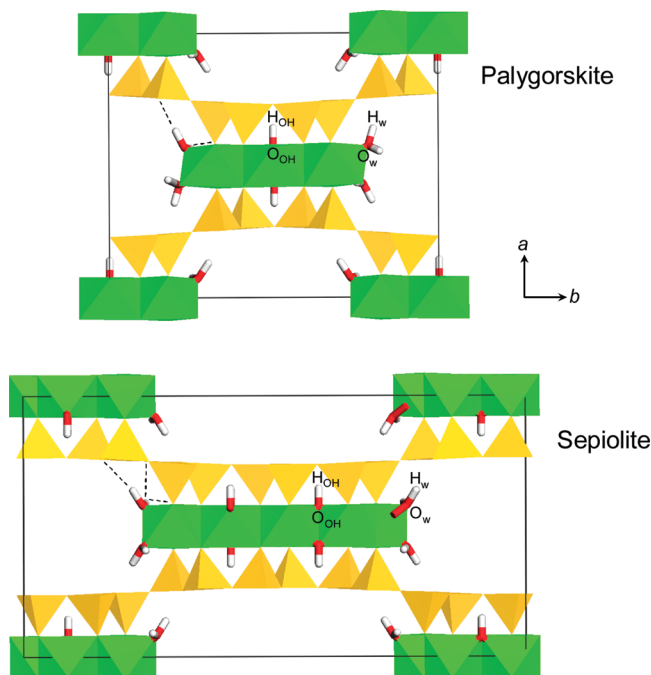
Figure 1. Polyhedra models of the unit cells of palygorskite (top) and sepiolite (bottom) derived from VASP DFT optimizations. Yellow tetrahedra and green octahedra represent coordinated Si and Mg atoms, respectively. Structural water molecules and hydroxides are highlighted as cylinders (O is red, H is white). Abbreviations O_{OH} and H_{OH} refer to hydroxyl oxygen and hydrogen, while O_W and H_W refer to water oxygen and hydrogen. All other framework oxygen atoms are abbreviated O_F in the text. Selected hydrogen bonds associated with structural water are shown as dashed lines.

Palygorskite and sepiolite are neutral trioctahedral clays with channels that exhibit pore-like behavior. Their architectures are comprised of 2:1 modulated phyllosilicate layers that sandwich octahedral Mg-(O, OH) sheets between tetrahedral Si—O sheets (Figure 1) and have the idealized formula,[38] respectively, $Mg_5Si_8O_{20}(OH)_2 \cdot 8H_2O$ and $Mg_8Si_{12}O_{30}(OH)_4 \cdot 12H_2O$. Both minerals examined in this study have been mined for centuries because of their versatility in applications ranging from pharmaceuticals and fertilizers to pesticides, molecular sieving, and ultrafiltration.[30–37] The utility of these clay minerals arises from their large surface areas and microporous molecular architectures. In fact, it was well-known centuries ago that mixing palygorskite and indigo produced the intensely colored blue pigment that is now known as "Maya Blue".[39,40]

Unlike the 2:1 continuous two-dimensional sheets of most clay minerals, the sheets in palygorskite and sepiolite are inverted in a regularly repeating pattern. Palygorskite has a chain of single hexagonal silicate ring structures that comprise the magnesiosilicate layer fragments. The silicate inversion at the edge of the fragment maintains the regular two-dimensional silicate sheet, albeit with periodic undulations. In contrast, sepiolite has two full silicate ring chain structures that comprise the magnesiosilicate layer fragments, again with the edge-based silicate inversions maintaining the regular undulations of the two-dimensional silicate sheets. The undulating silicate sheets in both phases are connected through linking Si—O—Si bonds from the inverted silicate tetrahedra on adjacent magnesiosilicate fragments. This architecture produces well-defined channels which exhibit pore-like behavior similar to the large continuous pores and channels characteristic of zeolite minerals.[41,42] The resulting channels in palygorskite and sepiolite are aligned parallel to the magnesiosilicate fragments. We calculated the channels within anhydrous palygorskite as having dimensions 6.65 Å × 12.05 Å (measured from atom centers) or 3.61 Å × 8.59 Å (subtracting appropriate van der Waals radii),[43] while the channels of anhydrous sepiolite have calculated dimensions of 7.71 Å × 15.77 Å (measured from atom centers) or 4.67 Å × 12.29 Å (again subtracting appropriate van der Waals radii).[36,37,43] The octahedral sheets of both phases (in anhydrous systems) are terminated at the channels by unsaturated Mg coordination sites. In natural samples, however, these edge coordination sites are satisfied by coordinating water molecules, which we henceforth refer to as "structural water". These two clay minerals therefore represent a unique opportunity to investigate water behavior at "inner edges" in a controlled manner, especially compared with the complex pH-dependent chemistry of hydroxyl groups on the external edges and cleavage surfaces of other oxide- and silicate-based minerals.

Fundamentally, the behavior of nanoconfined water is controlled by the complex local equilibria which exist among all chemical components in the system, which is difficult to quantify. In addition to the framework interactions, there are four distinct types of interactions: (1) water—water, (2) water—framework hydroxyl, (3) water—framework oxygen, and (4) water—framework metal. In this study, we investigate the behavior of both the noncoordinated pore water and the strongly coordinated structural water. The effects of these interactions (hydrogen bonding, induced dipoles, and electrostatics) produce localized restrictions, which in turn alter the behavior and properties of nanoconfined water from that of bulk water.[44–46] Quantification of these complex interactions is nontrivial and

(25) Liu, L.; Faraone, A.; Mou, C. Y.; Yen, C. W.; Chen, S. H. *J. Phys.: Condens. Matter, Spec. Sect. Water Confined Geometries* **2004**, *16*, S5403.

(26) Klein, J.; Raviv, U.; Perkin, S.; Kampf, N.; Chai, L.; Giasson, S. *J. Phys.: Condens. Matter, Spec. Sect. Water Confined Geometries* **2004**, *16*, S5437.

(27) Webber, B.; Dore, J. *J. Phys.: Condens. Matter, Spec. Sect. Water Confined Geometries* **2004**, *16*, S5449.

(28) Crupi, V.; Majolino, D.; Migliardo, P.; Venuti, V. *J. Mol. Liq.* **2005**, *117*, 165.

(29) Wang, J.; Kalinichev, A.; Kirkpatrick, J. R. *J. Phys. Chem. B* **2005**, *109*, 14308.

(30) Van Scoyoc, G. E.; Serna, C.; Ahlrichs, J. L. *Am. Mineral.* **1979**, *64*, 216.

(31) Jones, B. F.; Galan, E. Sepiolite and Palygorskite. Hydrous Phyllosilicates. In *Mineralogy*; Bailey, S. W., Ed.; Mineralogical Society of America: Chantilly, VA, 1988; Vol. 19, p 631.

(32) Galan, E. *Clay Miner.* **1996**, *31*, 443.

(33) Galan, E.; Carretero, M. I. *Clay. Clay Miner.* **1999**, *47*, 399.

(34) Ruiz-Hitzky, E. *J. Mater. Chem.* **2001**, *11*, 86.

(35) Wang, Q. K.; Matsuura, T.; Feng, C. Y.; Weir, M. R.; Detellier, C.; Rutadinka, R. L.; Van Mao, R. L. *J. Membr. Sci.* **2001**, *184*, 153.

(36) Post, J. E.; Bish, D. L.; Heaney, P. J. *Am. Mineral.* **2007**, *92*, 91.

(37) Post, J. E.; Heaney, P. J. *Am. Mineral.* **2008**, *93*, 667.

(38) Gaines, R. V.; Skinner, H. C. W.; Foord, E. E.; Mason, B.; Rosenzweig, A. *Dana's New Mineralogy*, 8th ed.; Wiley: New York, 1997.

(39) José-Yacamán, M.; Rendón, L.; Arenas, J.; Serra-Puche, M. C. *Science* **1996**, *273*, 223.

(40) Chiari, G.; Giustetto, R.; Druzik, J.; Doehne, E.; Ricchiardi, G. *Appl. Phys. A: Mater.* **2008**, *90*, 3.

(41) Smith, J. V. In *Zeolite Chemistry and Catalysis*; Rabo, J. A., Ed.; ACS Monograph 171; American Chemical Society: Washington, DC, 1976.

(42) Breck, D. W. *Zeolite Molecular Sieves*; John Wiley & Sons Inc.: New York, 1974.

(43) Bondi, A. *J. Phys. Chem.* **1964**, *68*, 441.

(44) Ockwig, N. W.; Cygan, R. T.; Hartl, M. A.; Daemen, L. L.; Nenoff, T. M. *J. Phys. Chem. C* **2008**, *112*, 13629.

(45) Ockwig, N. W.; Cygan, R. T.; Criscenti, L. J.; Nenoff, T. M. *Phys. Chem. Chem. Phys.* **2008**, *10*, 800.

requires a full complement of experimental and modeling techniques. Computer simulations, theoretical analyses, and experiments on the modified properties of nanoconfined water in restrictive local environments have been performed on virtually every class of porous material from aluminosilicates (i.e., clay minerals,[47,48] various silica gels and glass,[49−51] and zeolites[19,44−49]), porous carbons,[52] and polymers.[53] Previous studies from our research group incorporated experimental and classical modeling techniques to compare and partially explain the selectivity of three-dimensional framework molecular sieves and zeolites.[44−46]

Although a complete review of methods to probe bulk and nanoconfined water is beyond the scope of this paper, it is important to highlight the most commonly used techniques. Experimental evaluation of structural properties typically relies on neutron scattering[54] and X-ray diffraction,[55] while simulation methods include density functional theory (DFT), ab initio methods, grand canonical Monte Carlo (GCMC), and to some extent classical molecular dynamics (CMD). Complementary to structural characteristics, spectroscopic techniques provide details about the dynamic intra- and intermolecular behavior of nanoconfined water. These experimental techniques include Raman scattering,[56] microwave and IR spectroscopies,[57] quasi-elastic and inelastic neutron scattering (QENS and INS, respectively),[44−46,49−51,58,59] and nuclear magnetic resonance (NMR).[46,60] Ab initio and classical molecular dynamics (AIMD and CMD, respectively)[44−46,61−65] and DFT optimization can be used to evaluate and, ideally, be correlated with experimental spectroscopic results.

In this study we investigate changes in the behavior of nanoconfined molecular water through experimental and simulation techniques to evaluate the spectroscopic signatures arising from intermolecular interactions within the pores of the polysomatic clay minerals—palygorskite and sepiolite. These two particular phases were specifically targeted to avoid significant nonsystematic structural variations which would dramatically complicate analysis. However, direct comparison of palygorskite and sepiolite still enables us to focus on the fundamental questions relating to the impact of pore metrics, inner edge coordination sites, hydrogen bonding, and constricted geometries on the behavior of nanoconfined water.

Methods

Inelastic Neutron Scattering. The INS data were collected on the Filter Difference Spectrometer (FDS) at the Los Alamos Neutron Science Center (LANSCE) using a large three steradian (9848.4° ^{2}) solid-angle detector.[66−69] Samples of palygorskite (PFl-1)[37] and sepiolite (SepNev-1)[37] were obtained from the Source Clay Repository maintained by The Clay Mineral Society. To ensure that the samples were fully hydrated, each was placed in an 85 °C hydration chamber for 24 h prior to INS data collection.

A highly specialized technique, INS is ideally suited to examine any hydrogen-containing component of complex chemical systems and is particularly sensitive to the intermolecular rotational/librational motions which occur in the low-frequency (300−1100 cm^{-1}) region of the spectrum. Two distinct advantages of using INS are the lack of any spectroscopic selection rules and the highly selective sensitivity to protons with minimal contributions (generally) from non-hydrogen species (i.e., Mg, Si, O, Al, Fe, and Ca). *Molecular* motions which have nonzero angular moment appear in the librational region of the INS data, and restrictions of these motions due to local molecular environment are manifested by shifts in librational frequencies and peak shapes.[70−72] In the case of molecular water,[73] it is accepted that there are three distinct normal rotational modes (rocking, twisting, and wagging) which are broad and quite difficult to differentiate from one another. The lack of distinction between these finite modes arises from a multitude of coexisting and nondegenerate, but energetically localized, configurations, and this precludes the accurate correlated normal-mode analysis of many INS spectra. Librational modes are highly dependent on the local environment, position, and ordering. Occasionally sharp librational features can be observed when a hydrogen-containing component is very highly ordered, but typically a confluence of similar libration modes produces extremely broad (∼500 cm^{-1}) features which render most data sets challenging to interpret. Despite significant efforts, the absolute assignment of discrete wagging, twisting, and rocking modes remains problematic. Notwithstanding, it is well documented that librational frequencies increase and peak widths decrease as hydrogen bonding,[73] electrostatic, or steric restrictions[44,45] to the rotation are increased. The onset of the librational features in INS spectra is referred to as the librational edge and is often the only definitive spectroscopic assignment reported in INS experiments. However, even merged, the intensities of the soft librational features are significant and can be quantitatively predicted because of the relative simplicity of neutron−nucleus interactions.[74−76]

(46) Nenoff, T. M.; Ockwig, N. W.; Cygan, R. T.; Alam, T. M.; Leung, K.; Pless, J. D.; Xu, H.; Hartl, M. A.; Daemen, L. L. *J. Phys. Chem. C* **2007**, *111*, 13212.

(47) Soper, A. K. In *Hydrogen Bond Network*, Bellissent-Funel, M. C., Dore, J. C., Eds.; NATO ASI Series C: Mathematical and Physical Science; Kluwer Academic: Dordecht, 1994.

(48) Crupi, V.; Majolino, D.; Migliardo, P.; Venuti, V.; Wanderlingh, U.; Mizota, T.; Telling, M. *J. Phys. Chem. B* **2004**, *108*, 4314.

(49) Crupi, V.; Majolino, D.; Migliardo, P.; Venuti, V.; Wanderlingh, U.; Mizota, T.; Telling, M. *J. Phys. Chem. B* **2002**, *104*, 10884.

(50) Crupi, V.; Majolino, D.; Migliardo, P.; Venuti, V.; Diaonoux, A. *J. Appl. Phys.* **2002**, *74*, S555.

(51) Bellissent-Funel, M. C.; Lal, J.; Bosio, L. *J. Chem. Phys.* **1993**, *98*, 4246.

(52) Bellissent-Funel, M. C.; Dorbez-Sridi, R.; Bosio, L. *J. Chem. Phys.* **1996**, *104*, 1.

(53) Wiggins, P. M. *Prog. Polym. Sci.* **1988**, *13*, 1.

(54) Crupi, V.; Majolino, D.; Migliardo, P.; Venuti, V.; Bellissent-Funel, M. C. *Mol. Phys.* **2003**, *101*, 3323.

(55) Fourzi, A.; Dorbez-Sridi, R.; Oumezzine, M. *J. Chem. Phys.* **2002**, *116*, 791.

(56) Crupi, V.; Magazu, S.; Maisano, G.; Majolino, D.; Migliardo, P. *J. Mol. Liq.* **1999**, *80*, 133.

(57) Kaatze, U.; Uhlendorf, V. *Z. Phys. Chem.* **1981**, *126*, 151.

(58) Kolesnikov, A. I.; Li, J. C. *Physica B* **1997**, *234*, 34, and references therein.

(59) Venturini, F.; Gallo, P.; Ricci, M. A.; Bizzari, A. R.; Cannistraro, S. *J. Phys. Chem.* **2001**, *114*, 10010.

(60) Polnazek, C. F.; Bryant, R. G. *J. Phys. Chem.* **1984**, *81*, 4038.

(61) Gallo, P.; Ricci, M. A.; Rovere, M. *J. Chem. Phys.* **2002**, *116*, 342.

(62) Gallo, P.; Rapinesi, M.; Rovere, M. *J. Chem. Phys.* **2002**, *117*, 369.

(63) Murad, S.; Jia, W.; Krishnamurthy, M. *Mol. Phys.* **2004**, *102*, 2103.

(64) Demontis, P.; Stara, G.; Suffritti, G. B. *J. Chem. Phys.* **2004**, *120*, 9233.

(65) Shirono, K.; Endo, A.; Daiguji, H. *J. Phys. Chem. B* **2005**, *109*, 3446.

(66) Taylor, A. D.; Wood, E. J.; Goldstone, J. A.; Eckert, J. *Nucl. Instrum. Methods Phys. Res.* **1984**, *221*, 408.

(67) Sivia, D. S.; Vorderwisch, P.; Silver, R. N. *Nucl. Instrum. Methods Phys. Res.* **1990**, *A290*, 492.

(68) Specifications available: lansce.lanl.gov/Lujan/instruments/FDS/pdfs/FDS.pdf.

(69) Mitchell, P. C. H.; Parker, S. F.; Ramirez-Cuesta, A. J.; Tomkinson, J. *Vibrational Spectroscopy with Neutrons: With Applications in Chemistry, Biology, Materials Science and Catalysis*; World Scientific: River Edge, NJ, 2005; Vol. 3.

(70) Parise, J. B. In *Reviews in Mineralogy and Geochemistry: Neutron Scattering in Earth Sciences*; Wenk, H. R., Rosso, J. J., Eds.; Mineralogical Society of America: Washington, DC, 2006; Vol. 63.

(71) Line, C. M. B.; Kearley, G. J. *J. Chem. Phys.* **2000**, *112*, 9058.

(72) Line, C. M. B.; Kearley, G. J. *J. Chem. Phys.* **1998**, *234*, 207.

(73) Li, J. C. *J. Chem. Phys.* **1996**, *105*, 6733.

(74) Yildrim, T. *Chem. Phys.* **2000**, *261*, 205.

(75) Payne, M. C.; Teter, M. P.; Arias, D. C.; Joannopoulos, J. D. *Rev. Mod. Phys.* **1992**, *64*, 1045.

Density Functional Theory and ab Initio Molecular Dynamics. Periodic plane-wave DFT calculations were performed with the Vienna ab initio simulation package (VASP).[77,78] Frozen-core electronic states were described using the accurate projector-augmented wave (PAW) approach,[79,80] while electron exchange and correlation were treated within the generalized gradient approximation (GGA) according to Perdew–Wang.[81] Plane waves were included up to a 600 eV cutoff for geometry optimization and a 400 eV cutoff for AIMD simulation, and the Brillouin-zone sampling was restricted to the Γ point.

Initial structures were taken from the published crystal structures: palygorskite has lattice constants $a = 13.24$ Å, $b = 17.89$ Å, $c = 5.21$ Å, $\alpha = \gamma = 90.0°$, $\beta = 74.8°$, and space group $C2/m$ (No. 12);[82,83] sepiolite has lattice constants $a = 13.405$ Å, $b = 27.016$ Å, $c = 5.275$ Å, $\alpha = \beta = \gamma = 90.0°$, and space group $Pncn$ (No. 52).[36] Ignoring impurities and octahedral Al, or vacancy sites reported in some samples of playgorskite,[37] the idealized unit cell formulas are $Mg_{10}Si_{16}O_{40}(OH)_4 \cdot 16H_2O$ and $Mg_{16}Si_{24}O_{60}(OH)_8 \cdot 24H_2O$ for palygorskite and sepiolite, respectively.[36,82] One unit cell for each mineral phase was used. In each case pore waters were ignored for computational efficiency but structural waters (those coordinated to "inner edge" Mg atoms) remained. The dynamic nature of water prohibits an effective geometry optimization of these clays with pore waters. The resulting potential-energy minimum is so broad that realistic energy-minimized structures were not found.

Each model was first subjected to geometry optimization, in which all lattice parameters and atomic coordinates were varied. The resulting structures were then used as input for AIMD simulations at 300 K with a time step of 0.5 fs. Initially, 12.5 ps of *NVE* (N = number of particles, V = volume, E = potential energy) dynamics was followed by 50.0 ps of *NVT* (T = temperature) dynamics. Trajectory data from the final 25.0 ps of *NVT* simulation was used for averaging and vibrational analysis. The TINKER software suite[84] was used to obtain the velocity autocorrelation function (VACF) for each atom type as follows

$$C(t) = \frac{1}{N} \sum_{j=1}^{N} [v_j(0) \cdot v_j(t)] \qquad (1)$$

where $C(t)$ is the normalized summation of the dot products of atomic velocity, $v_j(t)$, relative to an initial velocity, $v_j(0)$. The summation in eq 1 runs over the number of atoms N of a given atom type or the entire set of atoms for a total VACF. The frequency-based power spectrum was calculated by squaring the Fourier-transformed VACF. Sampling every 2.0 fs in eq 1 ensured that vibrational frequencies up to 8000 cm^{-1} were captured, and a windowing gap of 6.0 ps was used to give a resolution of approximately 2.8 cm^{-1}. Separate VACF and power spectra were obtained for each atom type and an "all atom" power spectrum. This is an established approach to AIMD simulations of clay minerals to obtain structural and vibrational properties.[85]

Classical Molecular Dynamics. CMD simulations were performed with the LAMMPS software suite.[86] Consistent with our recent simulation studies of sodalite,[87] clinoptilolite,[44,45] and heulandite,[44,45] the atomic interactions of framework atoms are evaluated through nonbonded potentials and do not have fixed positions. Here, a nonbonded force field (CLAYFF) was used to describe all atomic interactions except for the hydroxyl groups, which required the addition of a bond stretch term.[88] Nonbonded van der Waals interactions are modeled through 6–12 Lennard–Jones potential terms,[89] while the electrostatics are modeled through Coulombic potential terms and handled through an Ewald summation method.[90] This allows for dynamic framework motions without imposing any rigid body restrictions and allows for an increased computational efficiency without using explicitly defined framework bonding parameters. The general nature of the CLAYFF force field is further enhanced by inclusion of a flexible SPC-based water model,[91] which has harmonic bending and stretching terms included. These bending and stretching terms are the only explicitly defined bonded interactions utilized in the force field.

The nonbonding potential energy, $E_{nonbond}$, between two atoms i and j separated by a distance r consists of electrostatic and Lennard–Jones terms given by eq 2

$$E_{nonbond} = \frac{q_i q_j}{4\pi\varepsilon_0 r} + 4\varepsilon_{ij}\left[\left(\frac{\sigma_{ij}}{r}\right)^{12} - \left(\frac{\sigma_{ij}}{r}\right)^6\right] \qquad (2)$$

where q_i and q_j are atomic charges, ε_0 is the dielectric permittivity of vacuum, ε_{ij} represents the well depth for Lennard–Jones attraction, and σ_{ij} is the Lennard–Jones diameter of the atomic pair. Arithmetic combination rules are used when $i \neq j$, such that $\varepsilon_{ij} = (\varepsilon_i\varepsilon_j)^{1/2}$ and $\sigma_{ij} = 1/2(\sigma_i + \sigma_j)$. The partial charges of "inner edge" Mg atoms were slightly adjusted to +1.5020 e and +1.4905 e (e is the elementary charge) for palygorskite and sepiolite, respectively, to maintain charge neutrality of the individual systems. CMD models without pore water had identical formula as described above in the DFT and AIMD section, while those with pore water (i.e., fully hydrated) had unit cell formulas of $Mg_{10}Si_{16}O_{40}(OH)_4 \cdot 16H_2O$ and $Mg_{16}Si_{24}O_{60}(OH)_8 \cdot 24H_2O$ for palygorskite and sepiolite, respectively. Because LAMMPS is currently only compatible with orthonormal systems, palygorskite was converted into an orthorhombic cell. The models of both phases were expanded to primitive ($P1$) supercells of similar size. The palygorskite supercell included 165 primary units cells (expanded to $5 \times 3 \times 11$) containing a total of 20 130 atoms and 2640 waters, while the sepiolite supercell contained 80 primary unit cells (expanded to $4 \times 2 \times 10$) containing a total of 15 040 atoms and 1920 waters.

First, constant-pressure simulations (*NPT* ensemble) were performed with a target pressure and temperature of 0 atm and 300 K, respectively. Barostatic and thermostatic relaxation times were both set at 100 fs. In each case, snapshots from the *NPT* simulation (Figure 2) with lattice parameters close to their average equilibrium values were used as initial configurations for constant-volume simulations (*NVT* ensemble). Short-range interactions were evaluated every 0.5 fs with a real-space cutoff of 10.0 Å. Long-range electrostatic interactions were evaluated every 1.0 fs using the particle–particle particle–mesh (pppm) summation algorithm[92] with a precision of 1.0×10^{-4}. For both *NPT* and *NVT* simulations, an equilibration stage of 250 ps was followed by a production stage

(76) Lovesey, S. *Theory of Neutron Scattering in Condensed Matter*, 3rd ed.; Oxford University Press: New York, 1987.
(77) Kresse, G.; Furthmuller, J. *Comput. Mater. Sci.* **1996**, *6*, 15.
(78) Kresse, G.; Furthmuller, J. *Phys. Rev. B* **1996**, *54*, 11169.
(79) Kresse, G.; Joubert, D. *Phys. Rev. B* **1999**, *59*, 1758.
(80) Blochl, P. E. *Phys. Rev. B* **1994**, *50*, 17953.
(81) Perdew, J. P.; Wang, Y. *Phys. Rev. B* **1992**, *45*, 13244.
(82) Chisholm, J. E. *Can. Mineral.* **1992**, *30*, 61.
(83) Chisholm, J. E. *Can. Mineral.* **1990**, *28*, 329.
(84) *TINKER: Software Tools for Molecular Design*, Version 4.2; 2004; http://dasher.wustl.edu/tinker/.
(85) Larentzos, J. P.; Greathouse, J. A.; Cygan, R. T. *J. Phys. Chem. C* **2007**, *111*, 12752.
(86) Plimpton, S. J. *J. Comput. Phys.* **1995**, *117*, 1.
(87) Moloy, E. C.; Cygan, R. T.; Bonhomme, F.; Teter, D. M.; Navrotsky, A. *Chem. Mater.* **2004**, *16*, 2121.
(88) Cygan, R. T.; Liang, J. J.; Kalinichev, A. G. *J. Phys. Chem. B* **2004**, *108*, 1255.
(89) Lennard-Jones, J. E. *Proc. Phys. Soc.* **1931**, *43*, 461.
(90) Fraser, L. M.; Foulkes, W. M. C.; Rajagopal, G.; Needs, R. J.; Kenny, S.; Williamson, A. J. *Phys. Rev. B* **1996**, *53*, 1814.
(91) (a) Berendsen, H. J. C.; Postma, J. P. M.; van Gunsteren, W. F.; Hermans, J. In *Intermolecular Forces*; Pullmann, B., Ed.; Reidel: Dordrecht, 1981; p 331. (b) Teleman, O.; Jonsson, B.; Engstrom, S. *Mol. Phys.* **1987**, *60*, 193.
(92) Plimpton, S. J.; Pollock, R.; Stevens, M. *Eighth SIAM Conference on Parallel Processing for Scientific Computing*; Minneapolis, MN, 1997.
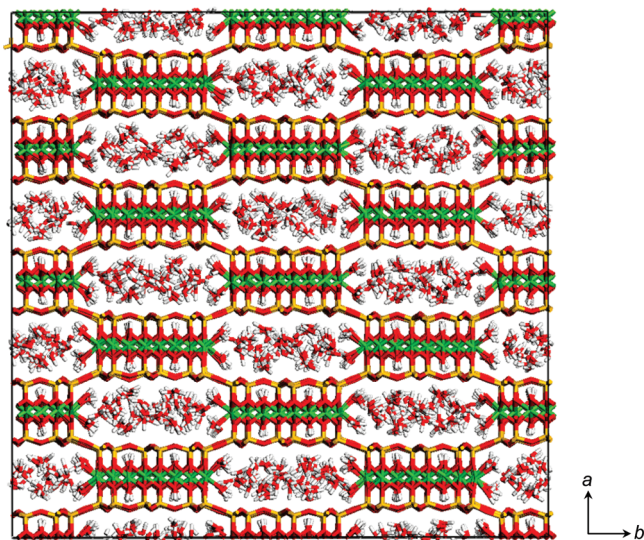
Figure 2. Snapshot image of the fully hydrated sepiolite structure obtained from the equilibrated trajectory associated with the CMD simulation. Water molecules occur in the sepiolite channels and coordinated to the edges of the magnesium sheets. Hydroxyls are disposed normal to the magnesium sheets. The color scheme is the same as in Figure 1. An equivalent simulation cell was used for palygorskite.

(1000 ps) for structural analysis with a data collection frequency of 0.5 ps. A final 40 ps *NVT* stage was used for VACF calculations, and the subsequent vibrational analysis was identical to that used for the AIMD trajectories.

Results

Inelastic Neutron Scattering. The INS spectrum of each hydrated clay mineral sample (PFl-1 and SepNev-1, palygorskite and sepiolite, respectively) was measured to specifically examine the *inter*molecular interactions of water as observed by changes in the librational (rotational) spectrum. When confined on a molecular scale, the behavior of water is modified from that of the bulk in spectroscopically measurable ways. There are two fundamentally different types of modifications observed in vibrational spectra. First, a direct modification of the *inter*molecular interactions which is observed as strongly shifted (>50 cm^{-1}) librational/rotational (300−1100 cm^{-1}) modes. Second, induced changes where the *intra*molecular bending (∼1600 cm^{-1}) and stretching (3300−3700 cm^{-1}) modes have relatively subtle shifts (<15 cm^{-1}) due to the local coordination environment and hydrogen bonding.

Variable-temperature studies were performed, and the INS data indicate a statistically insignificant difference in both peak intensities and positions; therefore, we only present the 90 K data (Figure 3). It should also be noted that despite our best efforts at ensuring bulk dryness, there is undoubtedly some contribution from water adsorbed on the external surfaces of the phyllosilicate samples used in the data collection. For calibration purposes, scattering data of ice I$_h$ was collected both before and after the samples were run and showed no appreciable deviation. Comparison of the INS data from the two minerals shows a dramatic shift between the librational features of each of the phases. In the INS spectra we observe librational edges at approximately 358 cm^{-1} for palygorskite and 536 cm^{-1} for sepiolite. These results clearly indicate less restricted water motion in the smaller-pore palygorskite (lower frequencies) than the larger-pore sepiolite (higher frequencies). Additionally, we observe almost no common INS spectral characteristics between
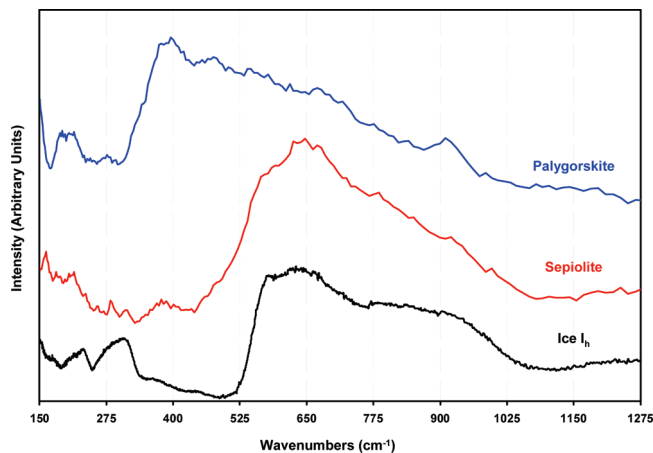

Figure 3. Inelastic neutron scattering (INS) data of fully hydrated palygorskite (blue), sepiolite (red), and ice I$_h$ (black)[44,45,58] at 90 K.

Table 1. Unit Cell Parameters from DFT Geometry Optimization, CMD Simulation, and Experiment

	palygorskite			sepiolite		
	DFT[a]	CMD[a]	experiment[82]	DFT[a]	CMD[a]	experiment[36]
a/Å	14.11	12.84 (4)	13.24	13.82	13.01 (3)	13.405 (1)
b/Å	17.40	18.03 (2)	17.89	26.52	26.78 (3)	27.016 (1)
c/Å	5.17	5.31 (1)	5.21	5.19	5.36 (1)	5.2750 (1)
α/deg	90.0	90.0	90.0	90.0	90.0	90.0
β/deg	81.9	68.3 (1)	74.8	90.0	90.0	90.0
γ/deg	90.0	90.0	90.0	90.0	90.0	90.0
V/Å^3	1257	1142 (4)	1190.89	1902	1867 (3)	1910.4 (1)

^{a} Simulated systems contain only structural water without pore water.

palygorskite and ice I$_h$ and a much greater similarity between the spectral data of sepiolite and ice I$_h$.

Simulated Structure. Lattice parameters from both CMD simulation (*NPT* ensemble) and DFT geometry optimization are presented in Table 1. The CMD simulations of sepiolite resulted in a 2−3% underprediction of the *a* and *b* lattice parameters and a roughly 2% overprediction of the crystallographic *c* axis, while DFT geometry optimization resulted in a 3% overprediction of the *a* axis and a 2% underprediction in *b* and *c*. The CMD results for palygorskite show good agreement with the observed lattice parameters and the DFT results. However, for palygorskite, DFT overpredicts the *a* axis by 6% while the other lattice parameters are in good agreement (1−2%). The *a*-axis value is most sensitive to the DFT energy cutoff; at 600 eV the optimized *a* axis underpredicts the crystallographic value by 7%. CMD calculations were performed at 300 and 90 K, while experimental data were collected at 90 K. However, the DFT results were obtained from geometry optimization, so thermal components are neglected. Furthermore, for computational efficiency the DFT model system contained only structural waters and not pore waters.

Examination of the local coordination environments about the Mg ions from simulations (without pore water) enables us to validate our classical force field parameters used in CMD, through comparison with the more rigorous but computationally expensive DFT results. The corresponding Mg−O distances from DFT geometry optimization and AIMD simulation are presented in Table 2. As in the DFT and AIMD results, the structural waters in the CMD simulations also maintain first-shell coordination positions around the "inner edge" Mg ions, even when the pore water is removed. Keeping in mind that both edge Mg and nonedge Mg ions were used to determine

Table 2. Comparison of Experimental and Simulation Mg−O Distances and First-Sphere Coordination Numbers (CN) in Palygorskite and Sepiolite

palygorskite					
Mg−O bond[a]	experimental[82]	DFT[b]	AIMD[c]	CMD[c]	CN[d]
Mg−O$_F$	2.03 (1)	2.10 (5)	2.10 (9)	2.05 (8)	3.97
Mg−O$_{OH}$	2.03 (1)	2.06 (4)	2.05 (8)	2.11 (7)	1.18
Mg−O$_W$	2.03	2.10 (3)	2.08 (7)	2.17 (9)	0.77

sepiolite					
Mg−O bond[a]	experimental[36]	DFT[b]	AIMD[c]	CMD[c]	CN[d]
Mg−O$_F$	2.08 (1)	2.09 (4)	2.065 (7)	2.07 (6)	4.00
Mg−O$_{OH}$	2.07 (1)	2.05 (3)	2.033 (5)	2.11 (8)	1.50
Mg−O$_W$	2.06 (1)	2.080 (1)	2.05 (1)	2.19 (6)	0.50

[a] O$_F$, O$_{OH}$, and O$_W$ represent framework oxygen, hydroxyl oxygen, and water oxygen, respectively. [b] Standard deviation calculated as the average of individual static bonds after geometry optimization. [c] Calculated using the PeakFit v4.12 software suite from MD simulations at 300 K. [d] Calculated from CMD results as the overall average across all unique Mg positions.

Mg−O coordination numbers, Table 2 illustrates that two water molecules are coordinated to each "inner edge" Mg ion. This is an encouraging result considering that no bonded terms were used for interactions between these Mg ions and water molecules and is consistent with the relatively large hydration energy associated with Mg^{2+}.[45] The only modification made to CLAY-FF parameters used in the CMD simulations was to adjust the atomic charge of these "inner edge" Mg atoms to +1.5020 e and +1.4905 e for palygorskite and sepiolite, respectively. Additionally, we anticipate that the nonbonded force field method could be used to describe doubly protonated hydroxyl (OH$_2^+$) groups coordinated to edge metal sites in other metal−oxide-based minerals which would be expected when exposed to low-pH aqueous solutions.

The DFT geometry-optimized structures of palygorskite and sepiolite systems without pore water (Figure 1) give some insight into differences in their vibrational behavior. In sepiolite, all silicate tetrahedra have a uniform orientation relative to the crystallographic a axis. There appears to be little strain in the corner-sharing siloxane oxygen atoms at the inversion point that joins adjacent magnesiosilicate fragments. The situation is very different for palygorskite, where the silicate tetrahedra are tilted with respect to the crystallographic a axis. As a result, the structural waters (and potentially the pore waters) in the two clay phases have very different hydrogen-bonding environments. In both cases, hydrogen bonds exist between the hydrogen atom of the water (H$_W$) and the inversion point O$_F$ atoms in the same octahedral sheet, although these bonds are shorter in palygorskite (1.9 Å) than sepiolite (2.2 Å). A similar hydrogen-bonding motif occurs between the H$_W$ and O$_F$ atoms from silicate tetrahedra on the adjacent sheet, but again, the bonds are slightly shorter in palygorskite (1.9 Å) than sepiolite (2.0 Å). However, only in sepiolite are H$_W$ atoms able to form a third hydrogen bond to the inversion point O$_F$ atoms, at a distance of 2.5 Å. As seen in Figure 1, the tilted silicate tetrahedra in palygorskite result in a much longer distance of 2.8 Å between these corresponding atoms (i.e., H$_W$ and inversion point O$_F$). Structural water molecules in sepiolite are therefore in a more constrained hydrogen-bonding environment than in palygorskite.

Simulated Spectra. Experimentally determined INS data are correlated with the rotational (librational) features of the hydrogen components (structural water, pore water, and hy-

droxyl) derived from molecular simulations for palygorskite and sepiolite. At both quantum and classical levels of theory, the simulated spectra (Figure 4) indicate differences in the water O−H peak structure between palygorskite and sepiolite. Looking first at the O−H stretching region (>3000 cm^{-1}), we see that both levels of theory result in clearly distinguishable peaks for layer O−H and water O−H stretching modes. However, the AIMD results show a much larger shift between layer O−H and water O−H stretching frequencies. The use of a harmonic O−H bond stretch potential in the CMD simulations is the likely cause of this discrepancy, as observed previously in studies of the clay Na−montmorillonite.[93] The harmonic potential used in CMD does an especially poor job predicting the symmetric and asymmetric water O−H stretching frequencies (3700−3800 cm^{-1}), while the AIMD frequencies (3200−3500 cm^{-1}) are in much better agreement with the experimentally observed values (ca. 3227 cm^{-1} for symmetric and 3490 cm^{-1} for asymmetric) for bulk water.[94] Through the CMD results we observe that water in palygorskite has two distinct peaks (3699 (8) and 3757 (5) cm^{-1}) corresponding to O−H stretching modes. The same pattern is present in the sepiolite data; however, the peaks are systematically shifted to higher frequencies (3707 (7) and 3768 (6) cm^{-1}). In contrast, the AIMD results illustrate that structural water in both palygorskite and sepiolite has only a single peak near 3500 cm^{-1} with a broad tail. A smaller peak at approximately 3350 cm^{-1} is visible above the tail and could be related to the second peak seen in the CMD spectra. Normal mode analysis using the DMol^3 software (Accelrys, Inc.) shows two O−H stretching modes for structural water in both clay phases, but in the power spectra the lower-frequency peak is barely distinguishable from the broad tail due to the thermal motion of these structural waters. The two distinct peaks in the CMD power spectra could indicate a unique O−H stretching frequency for structural water compared to pore water.

Water peaks below 1000 cm^{-1} correspond to *inter*molecular librational modes (i.e., wagging, rocking, and twisting), and this is the most critical region for comparison of INS spectra. DFT-optimized structures of these two clays indicate different hydrogen-bonding environments for the structural waters, which is a likely explanation for differences seen in the librational features of the INS spectra. Without pore waters, the AIMD spectra do not show a librational edge. The prominent peaks between 600 and 800 cm^{-1} are due to structural O−H groups and not water. However, the CMD results show marked differences in the librational edge at 374 and 448 cm^{-1} for palygorskite and sepiolite, respectively. The librational features are subtly different for the two individual clay minerals; variable-temperature molecular dynamics simulations exhibit only slightly shifted stretching frequencies, while the librational features remain largely unchanged.

Discussion

The simulated Mg−O distances closely match the experimental values, with several exceptions. The CMD results slightly overestimate the Mg−O$_{OH}$ and Mg−O$_W$ distances for both minerals, while the AIMD and DFT results overestimate the Mg−O$_W$ and Mg−O$_F$ distances for palygorskite. The results in Table 2 suggest that the presence of pore water has a direct influence on the Mg−O$_W$ bond lengths. However, at least at

(93) Greathouse, J. A.; Durkin, J. S.; Larentzos, J. P.; Cygan, R. T. *J. Chem. Phys.* **2009**, *130*, 134713.

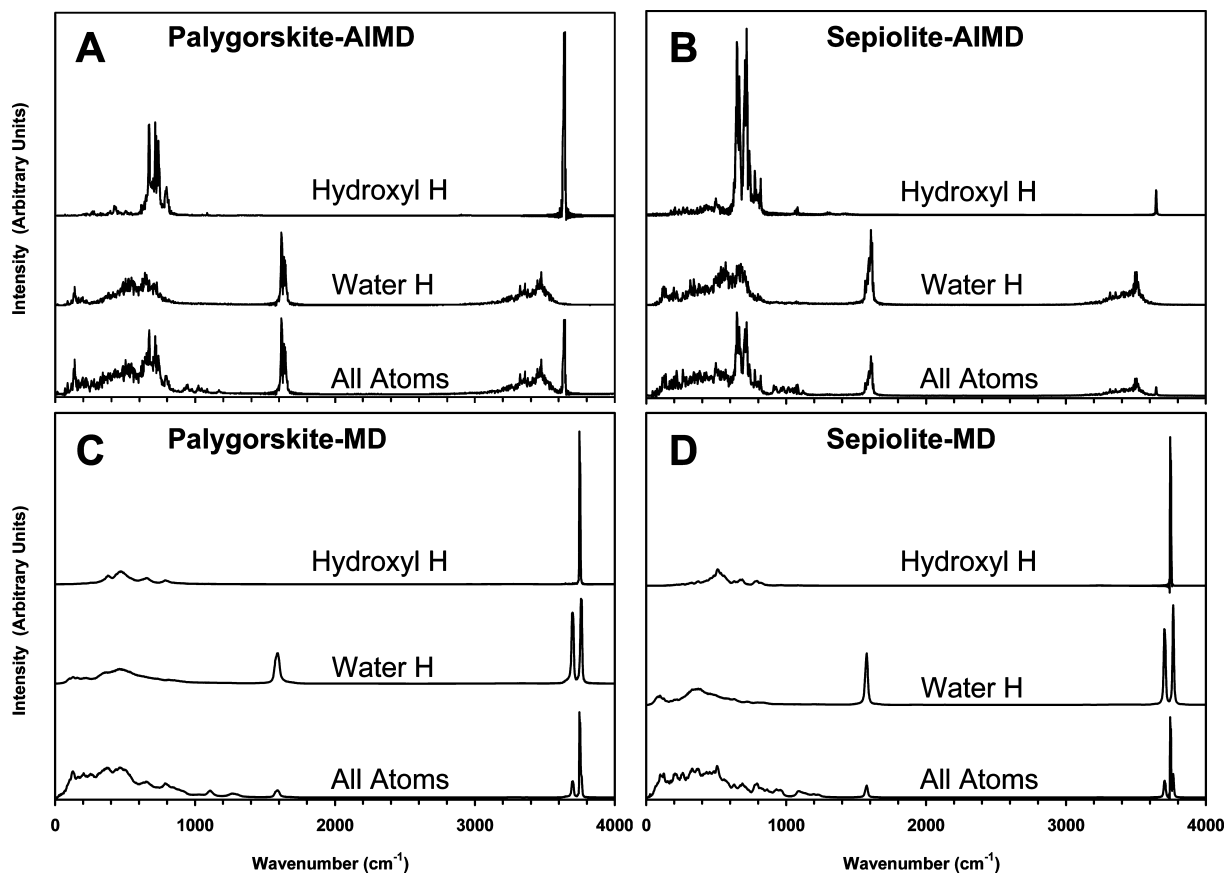(94) Walrafen, G. E.; Pugh, E. *J. Solution Chem.* **2004**, *33*, 81.

Figure 4. Hydroxyl H, water H, and all atom (without pore waters) power spectra at 300 K of (A) AIMD palygorskite, (B) AIMD sepiolite, (C) CMD palygorskite, and (D) CMD sepiolite.

Table 3. Comparison of 90 K CMD Simulation Mg−O Distances and First-Sphere Coordination Numbers (CN) for Palygorskite and Sepiolite with and without Pore Water

	palygorskite			
	with pore water		without pore water	
Mg−O bond[a]	MD[b]	CN[c]	MD[b]	CN[c]
Mg−O_F	2.05 (8)	3.97	2.03 (3)	3.99
Mg−O_OH	2.11 (7)	1.18	2.11 (3)	1.19
Mg−O_W	2.17 (9)	0.77	2.18 (1)	0.77

	sepiolite			
	with pore water		without pore water	
Mg−O bond[a]	MD[b]	CN[c]	MD[b]	CN[c]
Mg−O_F	2.07(7)	4.00	2.08(1)	4.00
Mg−O_OH	2.11(7)	1.50	2.12(1)	1.50
Mg−O_W	2.18(8)	0.50	2.18(1)	0.50

[a] O_F, O_{OH}, and O_W represent framework oxygen, hydroxyl oxygen, and water oxygen, respectively. [b] Calculated using the PeakFit v4.12 software suite. [c] Calculated as the overall average across all unique Mg positions.

the CMD level, we know that this influence is nearly negligible as the Mg−O bond lengths for models with and without pore waters (see Table 3) are all within the standard deviation of one another and the experimental values for palygorskite. We conclude that the hydrogen bonding between the structural and pore water is much weaker than the Mg−H₂O interactions and therefore only has a minimal impact on bond lengths. The consistent overestimation of the Mg−O_W distances at the CMD level suggests a shortcoming of nonbonded parameters used in

the CMD simulations. Direct comparison of INS, CMD (with and without pore water), and AIMD (without pore water) data is the final evidence which allows for the correlations of trends found between the theoretical and experimental data (Figure 5). In particular, we focus on both the broad features of the INS data and the sharper features of the AIMD results. The INS librational edge for palygorskite is slightly overpredicted by the CMD results, while the observed INS librational edge for the larger-pore sepiolite is significantly underpredicted by the CMD results. The libration features for both "with pore" and "without pore" water models also show significant shifts in CMD simulations. However, when pore waters are included in the CMD simulations, we can clearly see that the moderately defined peaks become even less resolved and more challenging to differentiate. This is particularly evident with sepiolite. The dynamical behavior of a large ensemble of pore water molecules at finite temperatures, while forming and breaking hydrogen bonds, leads to this diffuse vibrational response.

When comparing the simulation results, it is important to remember that DFT and AIMD methods are much more computationally expensive than classical methods and therefore are only used on smaller systems. The AIMD simulations combine the quality of the DFT results with the deterministic and large sampling capacity of classical molecular dynamics. As can be seen in our calculations, the AIMD results show more highly isolated and distinguished bands of librational motions than those found in the CMD results. These differences are further affected by the fact that our DFT models do not contain pore waters, thereby further decreasing the number of water and hydrogen-bonding configurations which are sampled.
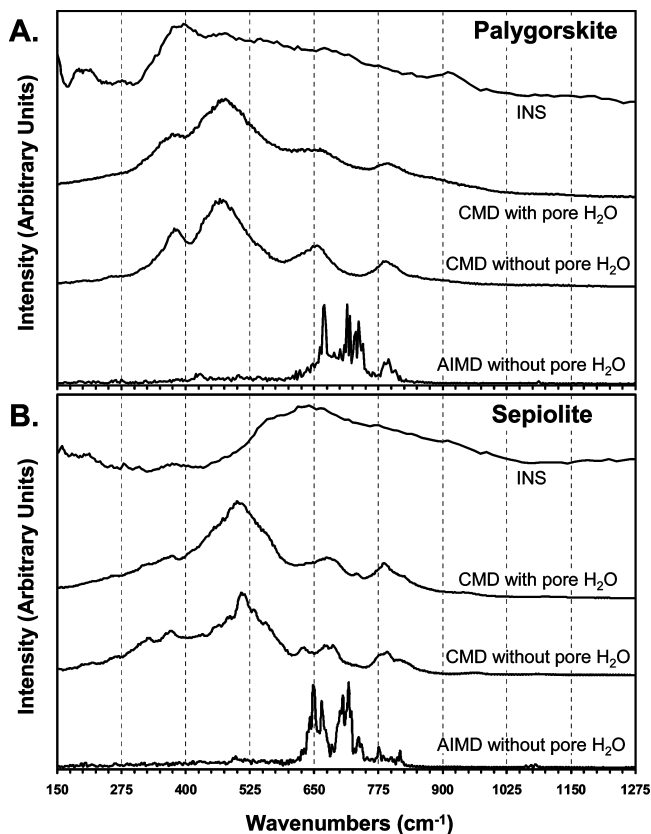
Figure 5. Comparison of experimental and simulated librational spectra of the hydrogen-containing components of (A) palygorskite and (B) sepiolite. All spectra correspond to 90 K except AIMD, which corresponds to 300 K.

The INS spectra, as expected for complex natural samples, exhibit the poorest resolution of peaks and have almost no clearly distinguishing features except for the shift observed in the librational edges. Because librational frequencies increase as a function of hydrogen-bonding extent, we conclude that sepiolite has more significant hydrogen bonding and restricted water motion than palygorskite. This characteristic behavior is observed across all experimental and theoretical results presented here. We interpret this response to be primarily related to the structural distortion of silicate tetrahedra at the inversion point between magnesiosilicate layer fragments. Tilting of the linking tetrahedra in palygorskite prevents the more efficient hydrogen bonding of the structural water molecules to the framework oxygen atoms as observed for sepiolite. The different hydrogen-bonding environments are related to the fundamental nature of magnesium-rich phyllosilicates and the strain associated with the coordination of magnesium octahedra between the silicate sheets. Compared to aluminum octahedra in most phyllosilicates, the larger magnesium octahedra in palygorskite and sepiolite create significant framework strain that leads to the characteristic layer inversions. Palygorskite—having a single chain of hex-

agonal silicate rings associated with the magnesiosilicate fragment, in contrast to the wider double hexagonal ring structure of sepiolite (see Figure 1)—must allow for significant tetrahedral tilt to accommodate the tetrahedra−octahedra mismatch.

Conclusions

Characterizing the behavior of water confined in nanoporous materials is crucial to advance our understanding of macroscopic phenomena. We utilized a combination of modeling/simulation and experimental studies to better understand the nature of occluded water in unidimensional-pored clays. Correlation of these complementary methods provides a strong basis to identify and explain the differences observed in the spectroscopic data of water in two relatively unique clay minerals. Distortions in the silicate tetrahedra effectively disrupt hydrogen-bonding patterns of the interfacial water and have greater impact on the dynamical behavior of nanoconfined water than the actual size of the pore or the presence of coordinatively unsaturated magnesium inner edge sites. These distortions in smaller-pore palygorskite interrupt the hydrogen-bonding network and ultimately produce a reduced number of hydrogen bonds between the coordinated water and the phyllosilicate lattice; these bonds are relatively short and correspondingly strong compared to typical hydrogen bonds associated with bulk water. In the absence of distorted silicate tetrahedra, as observed in the larger-pore sepiolite, a greater number of hydrogen bonds per structural water molecule are observed, although the bond distances are greater than those observed in palygorskite. Our simulations predict the relative frequency shift in the librational modes, and INS data clearly exhibit the higher frequency libration features of the larger-pore sepiolite. The hydrogen bonding of the pore waters at their interface dictates the experimental INS librational shifts. We conclude that distortions of the silicate tetrahedra in these particular clay minerals disrupts hydrogen-bonding patterns and have a greater impact on the dynamical behavior of nanoconfined water than the actual size of the pore or the presence of coordinatively unsaturated magnesium inner edge sites.